

ARTICLE TYPE

Quantum state encoding of vortical flows with the spinor field

Hao Su¹ | Shiying Xiong² | Yue Yang^{1,3}

¹State Key Laboratory for Turbulence and Complex Systems, School of Mechanics and Engineering Science, Peking University, Beijing, China

²Department of Engineering Mechanics, School of Aeronautics and Astronautics, Zhejiang University, Hangzhou, China

³HEDPS-CAPT, Peking University, Beijing, China

Correspondence

Shiying Xiong
Email: shiying.xiong@zju.edu.cn
Yue Yang
Email: yyg@pku.edu.cn

Abstract

Encoding velocity fields as quantum states poses a significant challenge in the development of quantum algorithms for fluid dynamics. Conventional methods, often based on direct normalization of discrete velocity data, do not intrinsically capture the structure and dynamics of vortex flows, potentially introducing artifacts that affect accuracy in modeling flow evolution. We propose a method for encoding velocity fields as quantum states of a spinor field using the spherical Clebsch representation. By applying a pointwise normalization constraint, we develop an ansatz with parameterized controlled rotation gates, optimized through variational quantum algorithm. This approach encodes target velocity fields into spinor-based quantum states, offering a pathway to more efficient quantum simulations of fluid dynamics. Furthermore, the encoded quantum state can be mapped to the vortex-surface field, providing a useful approach for analyzing vortex dynamics and characterizing flow structures. While the calculation of loss function encounters exponential complexity per training step, and the measurement of all qubits is inevitable, leading to high computational complexity for implementation on quantum hardware and requiring further optimization, its effectiveness has been validated across various scenarios through quantum simulation. This method enables spinor-based encoding and quantum simulation, with potential applications to diverse vector fields and complex flows, including magnetohydrodynamics and reactive flows.

KEY WORDS

quantum computing, state preparation, variational quantum algorithm, vortex dynamics, spinor field

1 | INTRODUCTION

Quantum computing uses the principles of quantum mechanics, such as superposition and entanglement, to encode information and perform operations using qubits^{1,2,3,4}. Its potential to significantly accelerate specific computational problems has attracted researchers from a wide range of scientific fields^{5,6,7,8,9,10,11,12}. In particular, quantum computing of fluid dynamics (QCFD) is expected to be more efficient in specific scenarios, compared to classical computational fluid dynamics (CFD) methods^{13,14,15,16,17,18}. Several quantum computing algorithms have been developed for simulating fluid dynamics, including the study of one-dimensional (1D) steady inviscid Laval nozzle¹³, 1D steady channel flow¹⁹, and two-dimensional (2D) thermal convection²⁰.

Abbreviations: QCFD, quantum computing of fluid dynamics; VQA, variational quantum algorith.

One major challenge in applying quantum computing to fluid dynamics is the lack of a universal framework for encoding flow problems – represented by unconstrained vectors or tensors – into normalized quantum states. To address this, Meng and Yang^{21,22} proposed a method based on the hydrodynamic formulation of the Schrödinger equation. Their approach uses the quantum states of a spinor field^{23,24,25,26,27}, facilitated by a generalized Madelung transformation, to represent fluid mass density and velocity. The flow evolution is then approximated by propagating the wave function according to the hydrodynamic Schrödinger equation. This methodology has also been successfully implemented on a real quantum device to simulating an unsteady vortical flow²⁸.

The spinor exhibits elegant mathematical properties, combining an algebraic structure associated with the special unitary group $SU(2)$ and a geometric structure defined by the three-dimensional (3D) unit sphere. Specifically, the spin symmetry of the spinor maps to spatial directions in 3D Euclidean space through the Hopf fibration²⁹. This mapping enables the spinor to represent vortex lines as points on the Bloch sphere, offering an effective framework for visualizing and simulating vortical flows^{24,25,26,30}.

Despite its strengths, the current spinor-based method for a flow simulation requires a specified initial wave function field, which restricts its applicability in directly encoding velocity fields into quantum states. This constraint poses challenges for its integration with classical CFD approaches, which rely on velocity field representations. From the perspective of quantum computing, the key challenge lies in encoding the initial state for complex flow fields based on a given velocity field, a problem for which no general methods have yet been developed.

In this paper, we propose a spinor-based quantum encoding method to address this challenge by encoding velocity fields as quantum states using the spinor field and variational quantum algorithm (VQA)^{31,32}. This approach directly constructs a quantum state from a velocity field, enabling more practical applications in QCDF. The construction of the spinor field is formulated as an optimization problem subject to a normalization constraint, where the loss function establishes a connection between the spinor field and the velocity field. To implement this approach, we design a tailored quantum circuit that incorporates spinor field normalization using Hadamard gates and parameterized controlled rotation gates. Our method directly constructs the preparation circuit of the spinor field and the quantum states for Hamiltonian simulation from a given velocity field. By employing VQA-optimized quantum circuits, the number of quantum gates grows linearly with the number of qubits, thereby avoiding the exponential gate growth typical of existing general state preparation algorithms³³.

It should be mentioned that many studies also employ analytical decompositions for their state preparations, such as Pauli decomposition^{34,35} or general linear combination of unitaries (LCU) decomposition^{36,37,38}. These methods basically decompose a given quantum state into multiple states which can be conveniently prepared. However, in our case, the spinor field cannot be efficiently derived from a given velocity field and lacks uniqueness, as multiple distinct spinor fields may correspond to the same velocity field. Hence, analytical decomposition becomes impractical, and identifying spinor fields that can be efficiently prepared by quantum circuits is challenging. We therefore adopt a variational algorithm to bypass explicit spinor field construction and improve the likelihood of obtaining suitable quantum preparation circuits.

49 We also investigate the potential of quantum algorithms for simulating vortex dynamics. By using the con-
 50 structed spinor field as an initial condition within Meng's framework^{21,22}, we bridge quantum wave functions and
 51 classical fluid dynamics, particularly for vortical flows. This method enables the simulation of fluid velocity and
 52 density dynamics, offering new perspectives on vortex interactions.

53 This paper is structured as follows. Section 2 introduces the spinor field and describes the formulation of the
 54 optimization problem for its construction. Section 3 presents the detailed setup of the VQA for constructing the
 55 spinor field and its corresponding quantum circuit, along with a discussion on computational complexity. Section 4
 56 evaluates the algorithm of the proposed method using 1D Fourier series and 2D flow fields, as well as explores the
 57 application of quantum algorithms to simulate vortical flows. The conclusion and future works are presented in
 58 Section 5.

59 2 | METHODS

60 2.1 | Spinor field

61 The spinor here represents a two-component wave function for describing the quantum state of spin-1/2 particles,
 62 such as electrons^{39,40}. It takes the form $\psi = [\psi_1, \psi_2]^T$, where ψ_1 and ψ_2 are complex numbers. The squared
 63 magnitudes, $|\psi_1|^2$ and $|\psi_2|^2$, represent the probabilities of the system being in the spin-up and spin-down states
 64 along a chosen axis, respectively⁴¹. The spinor is required to be normalized, i.e., it satisfies

$$65 |\psi|^2 = \langle \psi, \psi \rangle_{\mathbb{R}} = 1. \quad (1)$$

66 Here, the inner product $\langle \cdot, \cdot \rangle_{\mathbb{R}}$ is defined as $\langle \psi, \phi \rangle_{\mathbb{R}} \equiv \text{Re}(\bar{\psi}_1 \phi_1 + \bar{\psi}_2 \phi_2)$, where $\bar{\psi}_i$ denotes the complex conjugate
 67 of ψ_i . While 3D vectors and frames are acted upon freely and transitively by 3D rotations, spinors transform under
 68 the action of the universal double cover of the rotation group. This transformation is expressible via exponentials
 69 of Pauli matrices, written as $e^{-\frac{i}{2}\theta\sigma_n}$, where σ_n is the unit vector in the direction of the rotation axis, and θ is the
 70 rotation angle. This matrix is an exponential of the Pauli matrix corresponding to the axis of rotation. Under a 360°
 71 rotation, the spinor does not return to its original state; instead, it acquires a phase factor, which is -1. Only a 720°
 72 rotation brings the spinor back to its initial state.

73 Algebraically, spinors are elements of the group $SU(2)$, the special unitary group in two dimensions, con-
 74 sisting of 2x2 unitary matrices with determinant 1. This group is the mathematical foundation for describing
 75 quantum states of spin- $\frac{1}{2}$ particles, such as electrons. Geometrically, spinors correspond to the unit 3-sphere \mathbb{S}^3 , a 3-
 76 dimensional manifold embedded in 4-dimensional space, defined by the equation $x_1^2 + x_2^2 + x_3^2 + x_4^2 = 1$. This space is
 77 fundamental in describing the continuous nature of spinor transformations. The Hopf fibration²⁹ maps $SU(2)$ onto
 78 the 2-sphere \mathbb{S}^2 , representing classical spin directions on the Bloch sphere. The Hopf fibration allows the 3-sphere
 79 to be viewed as a collection of circles, known as fibers, parameterized by points on the 2-sphere. This structure

positions $SU(2)$ as the "universal cover" of \mathbb{S}^2 , enabling it to represent all possible configurations of spin traditionally represented on the Bloch sphere. While spinors do not directly model fluid vorticity, a conceptual analogy to classical vortex dynamics emerges when interpreting spin vectors as sphere-valued Clebsch variables, which describe vorticity in fluid dynamics. In this context, spinors offer a compact and mathematically rich framework for encoding quantum states, establishing connections to classical fluid mechanics and vortical flow fields.

The spherical Clebsch representation⁴² provides a quantum-inspired method for describing velocity fields using a spinor field $\psi(\mathbf{x}, t) = [\psi_1(\mathbf{x}, t), \psi_2(\mathbf{x}, t)]^T$. Each component $\psi_i(\mathbf{x}, t) = a_i(\mathbf{x}, t) + i b_i(\mathbf{x}, t)$ for $i = 1, 2$ is a complex-valued function, where $a_i(\mathbf{x}, t)$ and $b_i(\mathbf{x}, t)$ are the real and imaginary parts, respectively, of each spinor component. This spinor field can be referred to as the spherical Clebsch wave function, emphasizing its role in representing velocity fields through the spherical Clebsch representation.

The connection between the spinor field and the velocity field in Euclidean space is given by

$$\mathbf{u}_\psi \equiv \hbar \langle \nabla \psi, i \psi \rangle_{\mathbb{R}} = \hbar(a_1 \nabla b_1 - b_1 \nabla a_1 + a_2 \nabla b_2 - b_2 \nabla a_2), \quad (2)$$

where \hbar is a constant that defines the quantization of vorticity, with its physical interpretation provided in Ref.²³. This equation illustrates how a velocity field can be interpreted as a quantum spin field encoded within the spinor framework.

Figure 1 illustrates a schematic of the vortex ring with different variable representations. In Fig. 1(a), the vortex tube is depicted as an isosurface of the vorticity magnitude, with vortex lines (integral curves of vorticity) superimposed on the surfaces to highlight the vortex structure. The direction of motion of the vortex tube is indicated by the blue arrow, and the semi-transparent background contours represent the component a_2 of the spinor field, demonstrating the link between the vorticity and spinor fields. In Fig. 1(b), the vortex tube is rendered semi-transparent to reveal its internal structure, and the contours are made opaque to emphasize the transformation of the velocity–vorticity field into the spinor field using the spherical Clebsch representation. This representation transforms the "tube-like" vortex structure into a "wave-like" spinor field, enabling its use in subsequent quantum computations.

Through the Hopf fibration, the spinor can be transformed into a spin vector $\mathbf{s} = (s_1, s_2, s_3)$ on the Bloch sphere⁴³, with

$$s_1 = a_1^2 + b_1^2 - a_2^2 - b_2^2, \quad s_2 = 2(a_2 b_1 - a_1 b_2), \quad s_3 = 2(a_1 a_2 + b_1 b_2). \quad (3)$$

Each component of \mathbf{s} corresponds to a vortex-surface field^{44,45} for the vorticity $\boldsymbol{\omega}_\psi \equiv \nabla \times \mathbf{u}_\psi$, with the constraint $\boldsymbol{\omega}_\psi \cdot \nabla s_i = 0$, $i = 1, 2, 3$. This mapping shows that each vortex line in physical space is associated with a point on the Bloch sphere, facilitating the visualization²⁴, prediction⁴⁶, and simulation^{25,26} of various vortical flows.

2.2 | Quantum algorithm

We aim to develop a quantum state preparation algorithm for calculating the spinor field ψ that satisfies Eq. (2) for a given velocity field. Nevertheless, it is usually not feasible to solve Eq. (2) directly⁴⁷, so we reformulate the

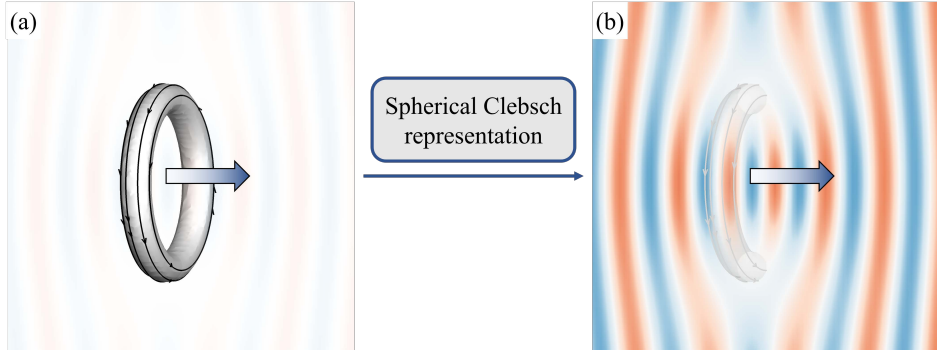


FIGURE 1 Schematic of a vortex ring in different mathematical forms. (a) The vortex tube is shown as an vorticity isosurface, with vortex lines overlaid on these surfaces. The motion of the vortex tube follows the direction indicated by the blue arrow. The semi-transparent background contours show the component a_2 of the spinor field. (b) The semi-transparent vortex tube and the opaque contours of a_2 highlight the conversion of the velocity–vorticity field into the spinor field through the spherical Clebsch representation.

112 inverse problem of Eq. (2) as an optimization problem

$$113 \quad \psi_u = \arg \min_{\|\psi\|=1} \frac{1}{\hbar^2} \|\mathbf{u}_\psi - \mathbf{u}\|_\epsilon^2, \quad (4)$$

114 where the norm $\|\cdot\|_\epsilon$ incorporates a regularization term²³ as

$$115 \quad \|\mathbf{u}_\psi - \mathbf{u}\|_\epsilon^2 = \|\mathbf{u}_\psi - \mathbf{u}\|^2 + \epsilon^2 \|\hbar \nabla s\|^2, \quad (5)$$

116 where $s = (s_1, s_2, s_3)$ is the spin vector defined as in Eq. (3). The regularizer $\epsilon^2 \|\hbar \nabla s\|^2$ enhances convexity of the
117 optimization to obtain a unique solution. We dynamically adjust ϵ to balance the solution accuracy and problem
118 regularization. Both the spinor field and the velocity fields are subjected to periodic boundary conditions in the
119 present study. Further discussion of the optimization problem in Eq. (4) is presented in Appendix A. For a more
120 geometrical perspective, the reader is referred to the work of Chern et al.²⁴

121 To solve the optimization problem Eq. (4) in a quantum algorithm, we discretize the velocity field and the spinor
122 field on a uniform grid. Within the VQA framework, we iteratively update parameters within quantum circuits to
123 obtain the target preparation circuit³¹.

124 Figure 2 illustrates the optimization process, starting from the default initial state $|0\rangle^{\otimes n}$ and iterating towards the
125 output spinor field $|\psi\rangle$. This is achieved by adjusting the parameters of a quantum circuit $U(\theta)$, with the evolution
126 described by $|\psi\rangle = U(\theta)|0\rangle^{\otimes n}$, where n denotes the number of qubits and $|0\rangle^{\otimes n}$ denotes the default initial state.
127 The circuit parameters θ are optimized using the AdamW algorithm⁴⁸, which minimizes a loss function $L(\cdot)$ that
128 depends on the target velocity input and the quantum output state. The loss function $L(\cdot)$ reaches its minimum when
129 the desired output state is achieved. Upon convergence of the algorithm, the resulting quantum state is obtained
130 and can be used for further simulation.

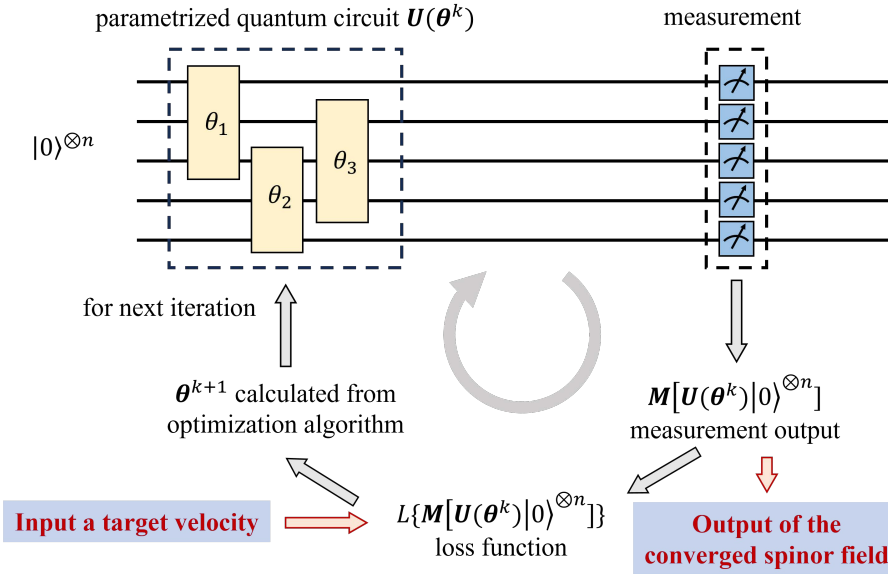


FIGURE 2 The optimization algorithm illustrates the iteration from the default initial state $|0\rangle^{\otimes n}$ to an output spinor field $|\psi\rangle$ via tuning a parameterized quantum circuit $\mathbf{U}(\boldsymbol{\theta})$, expressed as $|\psi\rangle = \mathbf{U}(\boldsymbol{\theta})|0\rangle^{\otimes n}$. The circuit parameters $\boldsymbol{\theta}$ are tuned using the AdamW optimization algorithm⁴⁸, optimizing with respect to a loss function $L(\cdot)$ that depends on the input target velocity. Here, $\boldsymbol{\theta}^k$ denotes the parameter values at the k -th iteration. After the algorithm converges, the target spinor field is obtained and can be used for further simulation.

131 The optimization is then formulated by varying parameters $\boldsymbol{\theta}$ to optimal ones

132

$$\boldsymbol{\theta}^{\text{opt}} = \arg \min_{\boldsymbol{\theta}} L\{\mathbf{M}[\mathbf{U}(\boldsymbol{\theta})|0\rangle^{\otimes n}]\} \quad (6)$$

133 to minimize the loss function, where \mathbf{M} represents the spinor field measurement. Note that the output of the
134 quantum circuit was obtained and the circuit parameters were optimized on a classical computer.

135 We define the loss function

136

$$L = \frac{1}{\hbar^2} \|\mathbf{u}_\psi - \mathbf{u}_t\|_\epsilon^2 \quad (7)$$

137 using a target velocity \mathbf{u}_t . This loss function corresponds to the optimization problem described in Eq. (4), where
138 ψ is obtained from the quantum circuit and can be converted into \mathbf{u}_ψ using Eq. (2). We then iteratively adjust $\boldsymbol{\theta}$
139 using the AdamW optimization algorithm⁴⁸ to minimize Eq. (7) and solve Eq. (4).

3 | IMPLEMENTATION OF THE QUANTUM ALGORITHM

3.1 | Encoding the spinor field

We consider a d -dimensional domain $[0, L_\Omega]^d$ with length $L_\Omega = 2\pi$, discretized by N^d uniform grid points. Spinors are defined at grid points $(i_1\Delta, i_2\Delta, \dots, i_d\Delta)$, where $\Delta = L_\Omega/N$ denotes the grid spacing and i_k ranges from 0 to $N - 1$ with $k = 1, 2, \dots, d$. These spinors, representing a discretized vector field, are encoded with n qubits. Specifically, one qubit is used to encode two spinor components, and the other $n - 1$ ones encode spinor positions, satisfying the condition $2^{n-1} = N^d$.

Following the encoding method of Meng and Yang²¹, we discretize a spinor field as

$$|\psi\rangle = \frac{1}{\mathcal{N}} \sum_{j_{n-2}=0}^1 \sum_{j_{n-3}=0}^1 \cdots \sum_{j_0=0}^1 [\psi_1(\mathbf{x}_j)|0\rangle + \psi_2(\mathbf{x}_j)|1\rangle] \otimes |j_{n-2}j_{n-3}\cdots j_0\rangle. \quad (8)$$

Here, the initial $n - 1$ qubits $|j_{n-2}j_{n-3}\cdots j_0\rangle$ encode the binary representation of the index j corresponding to the spatial coordinate \mathbf{x}_j . For each grid point at \mathbf{x}_j , the two components ψ_1 and ψ_2 are distinguished by the n -th qubit as $\psi_1(\mathbf{x}_j)|0\rangle + \psi_2(\mathbf{x}_j)|1\rangle$. The normalization coefficient $1/\mathcal{N}$ with $\mathcal{N} = \sqrt{2^{n-1}}$ ensures that the entire state has a unity norm.

3.2 | Designing quantum circuit for state preparation

In conventional quantum circuits, the global normalization condition is naturally satisfied, whereas the pointwise normalization expressed in Eq. (1) is generally not maintained for the spinor field. To bridge this gap, we develop a specialized quantum circuit architecture that preserves the pointwise normalization constraint for all variations of θ in the resulting spinor field. The designed quantum circuit is illustrated using a four-qubit system in Fig. 3. This circuit can be extended for more qubits with a similar structure.

The quantum circuit comprises a parameter-free Hadamard transformation and controlled rotation gates with adjustable parameters. First, we perform Hadamard transformations on $n - 1$ qubits, after which the quantum state becomes

$$|\psi\rangle = \frac{1}{\mathcal{N}} \sum_{j_{n-2}=0}^1 \sum_{j_{n-3}=0}^1 \cdots \sum_{j_0=0}^1 |0\rangle \otimes |j_{n-2}j_{n-3}\cdots j_0\rangle. \quad (9)$$

Recall that the spinor field should satisfy the normalization condition $|\psi|^2 = 1$, which means $|\psi_1(\mathbf{x}_j)|^2 + |\psi_2(\mathbf{x}_j)|^2 = 1$ for all j in Eq. (8). This implies that $|j_{n-2}j_{n-3}\cdots j_0\rangle$ has a probability magnitude of $1/\mathcal{N}$ for all possible j , which is guaranteed by the Hadamard transformations as in Eq. (9). After the transformation, most quantum gates applied on the first $n - 1$ qubits will destroy this normalization condition of spinor, thus no further operations are performed on them. The entire information of spinor field is considered to be encoded on the last qubit q_{n-1} , as $\psi_1(\mathbf{x}_j)$ and $\psi_2(\mathbf{x}_j)$ vary across different $|j\rangle$ states. To realize this distribution of different phases, we employ series of controlled rotation gates on the n -th qubit, with one of the former $n - 1$ qubits serving as the control qubit.

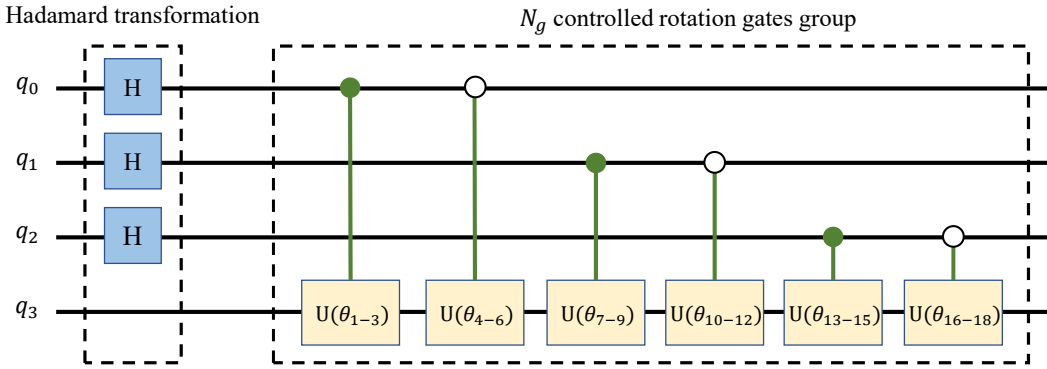


FIGURE 3 Schematic of a parameterized quantum circuit with enforced pointwise normalization in Eq. (1). The circuit employs Hadamard transformation and controlled rotation gates. The Hadamard transformations ensure the spinor normalization across $n - 1$ qubits. To maintain the normalization, no further operations are conducted on these qubits after the Hadamard transformation. Instead, controlled rotation gates are applied to the n -th qubit, so that the former $n - 1$ qubits serve as control qubits. The gate's action on the target qubit is controlled by $|1\rangle$ (solid circles) and $|0\rangle$ (open circles).

170 As shown in Fig. 3, we employ two types of control qubits to manipulate the rotation qubits, identified by solid
 171 and open circles, respectively. The gate applies the rotation matrix to the target qubit if the control qubit reads $|1\rangle$
 172 for the solid circle, and $|0\rangle$ for the open circle.

173 The controlled rotation gates, following the section consisting of Hadamard transformations, are general one-
 174 qubit controlled-unitary gates. All of them are 2×2 complex unitary matrices, each comprising three independent
 175 parameters. The arrangement of the controlled rotation gates is flexible. Here we organize these gates into multiple
 176 groups. Each group is generated by enumerating all possible control qubits, resulting in $2(n - 1)$ distinct gates. This
 177 group structure is then replicated N_g times and sequentially incorporated into the quantum circuit to increase the
 178 expressibility of the circuit. The selection of N_g is related to the complexity of the target velocity field and the qubit
 179 number, with examples provided in Tab. 1. For example, as shown in Fig. 3, where $n = 4$, if the gate grouping
 180 pattern is repeated $N_g = 2$ times, the circuit would contain a total of $2(n - 1)N_g = 12$ gates. The final state of this
 181 quantum circuit can be expressed as

$$182 |\psi\rangle = \frac{1}{\mathcal{N}} \sum_{j_{n-2}=0}^1 \sum_{j_{n-3}=0}^1 \cdots \sum_{j_0=0}^1 \prod_{p=1}^{(n-1)N_g} U_{2p-\Delta} |0\rangle \otimes |j_{n-2}j_{n-3} \cdots j_0\rangle.$$

183 where $\Delta = p \bmod (n - 1)$, and U_j refers to $U(\theta_{(3j-2)-(3j)})$ in Fig. 3. Basically, different combinations of unitary gates
 184 are implemented under different $|j\rangle$ states according to their binary representations.

185 An upper bound for N_g can be approximated by considering the degrees of freedom. An n -qubit pure state con-
 186 tains $2^n - 1$ independent numbers, while each controlled rotation gate contributes three free parameters. Therefore,

187 we can approximate the upper bound of N_g as

$$188 \quad N_g \leq \left\lceil \frac{2^n - 1}{6(n-1)} \right\rceil + 1. \quad (10)$$

189 However, it should be mentioned that this upper bound is not necessary for all scenarios. For example, Case 3 in
 190 Tab. 1 uses 11 qubits to encode a 2D velocity field with $N_g = 5$, while the upper bound yields $N_g \leq 35$, which
 191 is much larger than the actual number. This implies that the N_g depends on actual properties of the given velocity
 192 field.

193 3.3 | Complexity of the optimization algorithm

194 As illustrated in Fig. 3, for n qubits with N_g groups, the number of quantum gates in our circuit is

$$195 \quad N_q = 2(n-1)N_g \sim O(nN_g). \quad (11)$$

196 This is linear to n for a constant N_g , and it is exponentially smaller than the estimate of $N_q = O(4^n)$ for a general
 197 initial state⁴⁹.

198 We analyze the time complexity of our preparation algorithm. The grid, consisting of N^d points, is associated
 199 with n qubits, with the relation $2^{n-1} = N^d$. During each iteration, evaluating the loss function involves computing
 200 the gradient term $\nabla\psi$ in Eq. (5). The gradient is calculated using the central difference across all N^d grid points,
 201 requiring $O(N^d)$ operations. Therefore, the calculation of L takes $O(N^d)$ operations per step.

202 For each optimization step, gradient backpropagation is applied to every controlled rotation gate. Each gate
 203 operates on half of the total spinors, resulting in a time complexity of $O(N^dN_g)$ for a single step, where $O(N^d)$
 204 corresponds to the size of one group of the state space, and N_g is the number of gate groups. Over the entire training
 205 process, which involves N_i iteration steps, the total time complexity is $O(N^dN_gN_i)$. This computational effort is
 206 required only during the training phase and could potentially be improved through methods such as pretraining,
 207 which might enhance overall efficiency and reduce the computational cost.

208 Our algorithm demonstrates linear scalability in quantum gate count with respect to the number of qubits,
 209 highlighting its potential for efficient execution of trained quantum circuits on quantum hardware. However, there
 210 is still room for improvement in computational efficiency. Potential improvements include refining the loss function
 211 to enhance training efficiency and exploring alternative representations of the velocity field. Also, using parameter-
 212 shift rules⁵⁰ offers a practical and effective method to bypass direct calculation of $\nabla\psi$ term, which could help
 213 optimize the integration with quantum systems.

214 In addition, the evaluation and optimization of L in Eq. (7) require measuring the entire spinor field, which can
 215 be computationally demanding and may limit the feasibility of practical implementation on quantum hardware²,
 216 which usually require repeated measurements of all qubits in the register during each iteration step for loss function
 217 evaluation. We have explored the possibility of measurement speedup via Pauli decomposition numerically, as

218 presented in Appendix F. The result suggests that Pauli decomposition has the potential to reduce the measurement
 219 resource requirements during the early stages of optimization, where the loss function decreases the most quickly.

220 4 | COMPUTATIONAL RESULTS FOR VELOCITY ENCODING

221 We demonstrate the feasibility of our method through case studies in 1D ($d = 1$) and 2D ($d = 2$), with periodic
 222 boundary conditions. Detailed parameters and relative errors for all cases are listed in Tab. 1. We perform numerical
 223 optimization of circuit parameters using VQA on the Qiskit platform. To compute the gradients of the loss
 224 function L in Eq. (7) with respect to the parameters θ , we implement our method using the PyTorch framework,
 225 leveraging its automatic differentiation for gradient computation and the AdamW optimizer for parameter updates.
 226 This implementation has been validated for VQA training⁵¹.

227 During the training process, we use two different learning rate parameters, namely the initial learning rate ϵ_{lr1}
 228 and the final learning rate ϵ_{lr2} , which governs the step size of the optimization as defined in PyTorch. As listed in
 229 Tab. 1, the optimization process starts with ϵ_{lr1} and changes to ϵ_{lr2} when $L < 0.1$ for Case 1 and 2, while changes
 230 when $L < 10$ for Case 3 and 4. The regularization parameter ε begins at 1 and is reduced to 20% every 100
 231 iterations for Cases 1 and 2, and reduced to 10% every 1000 iterations for Cases 3 and 4.

232 The variation of loss function during the optimization process is presented in Fig. 4. It is observed that loss
 233 function decreases rapidly in the early stages of optimization, where a rough approximation of the spinor field can
 234 be obtained. To increase the accuracy of the result, the proceeding optimization process goes through a section
 235 of barren plateau, characterized by vanishing gradients^{52,53,54}, after which a better solution is acquired. The loss
 236 function for Cases 2 shows several sudden rises due to the reduction of the regularization coefficient ε .

237 Here, the average relative error is

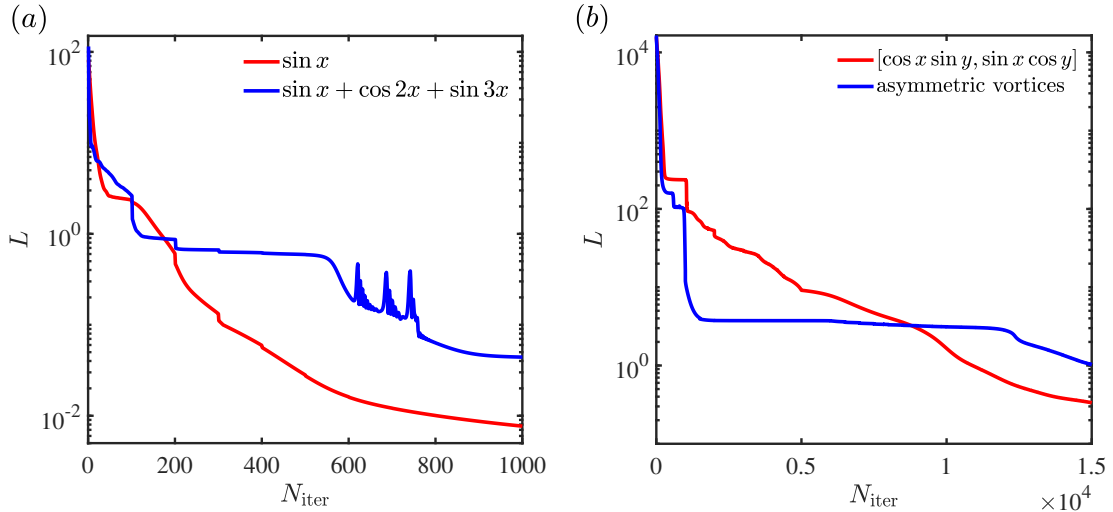
$$238 \quad \epsilon(\mathbf{u}_\psi, \mathbf{u}_t) \equiv \frac{\text{Avg}(|\mathbf{u}_\psi - \mathbf{u}_t|)}{\text{Avg}(|\mathbf{u}_t|)}, \quad (12)$$

239 where $\text{Avg}(\cdot)$ gives mean value over all grid points. This error measures the discrepancy between the spinor-based
 240 velocity \mathbf{u}_ψ and the target velocity \mathbf{u}_t . Furthermore, a sensitivity analysis with different parameter values is provided
 241 in Appendix C, along with a quantitative assessment of the circuit's expressibility in Appendix D.

242 It is worth mentioning that different initial relative errors might affect differently on evolution, dependent
 243 of properties of equations, difference schemes, time steps and so on. For example, for Schrödinger equation as
 244 discussed in Appendix B, the equation is linear, so the initial error will evolve in a controlled manner.

Case	\mathbf{u}_t	d	n	N_g	N	Ω	\hbar	N_{iter}	$\epsilon_{lr1}/\epsilon_{lr2}$	$\epsilon(\mathbf{u}_\psi, \mathbf{u}_t)$
1	$\sin x$	1	6	2	32	$[0, 2\pi]$	1	1000	0.03/0.015	3.83%
2	$\sin x + \cos 2x + \sin 3x$	1	6	2	32	$[0, 2\pi]$	1	1000	0.05/0.015	8.58%
3	$[\cos x \sin y, \sin x \cos y]$	2	11	5	32	$[0, 2\pi]^2$	1	15000	0.005/0.0003	4.50%
4	asymmetric vortices	2	11	6	32	$[0, 2\pi]^2$	1	15000	0.005/0.0003	37.53%

T A B L E 1 Parameters and errors in our testing cases, where \mathbf{u}_t (scalar fields for first two cases, and vector fields for last two cases) represents the target velocity, d denotes the number of dimensions, n the number of qubits, N_g the number of groups of controlled rotation gates, N the number of grid points along each dimension, Ω the computational domain, \hbar a factor associated with quantifying the vorticity field, N_{iter} the iteration steps, ϵ_{lr1} and ϵ_{lr2} the learning rates, and the relative error $\epsilon(\mathbf{u}_\psi, \mathbf{u}_t)$ is defined in Eq. (12). The learning rates decrease when $L < 0.1$ for the first two cases, and $L < 10$ for the last two cases.



F I G U R E 4 The variation of loss function for (a) Cases 1, 2 and (b) Cases 3, 4 in Tab. 1. The discontinuous rises of L are consequences of reduction in regularization coefficient ε .

245 4.1 | 1D velocity fields

246 We first consider a 1D target velocity field $u_t(x) = \sin x$. Note that 1D vectors will not be denoted in bold in
247 subsequent notation. This simple velocity field admits an analytic wave-function solution

$$248 \quad \psi_1 = \sin\left(\frac{x}{2} - \frac{\pi}{4}\right) e^{ix}, \quad \psi_2 = -\cos\left(\frac{x}{2} - \frac{\pi}{4}\right) e^{-ix} \quad (13)$$

249 to Eq. (2) for validating our state preparation method. In Fig. 5, the optimization method can construct continuous
250 spinor field, and approximate the target velocity field with a small relative error of 3.83%.

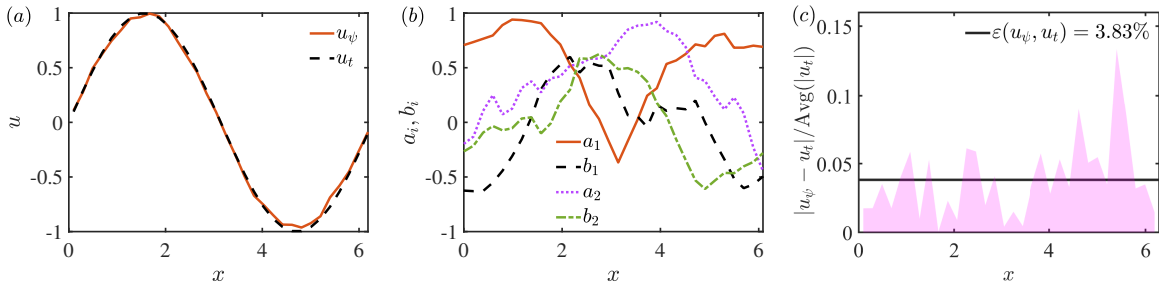


FIGURE 5 Results for generating the spinor field for $u_t = \sin x$. (a) Comparison between the target velocity u_t (black dashed line) and the quantum optimization result u_ψ (red solid line). (b) Four real components of the spinor $\psi = [a_1 + b_1 i, a_2 + b_2 i]^T$. (c) Relative error $|u_\psi - u_t| / \text{Avg}(|u_t|)$ (pink shade), with the average relative error $\varepsilon(u_\psi, u_t)$ (black solid line).

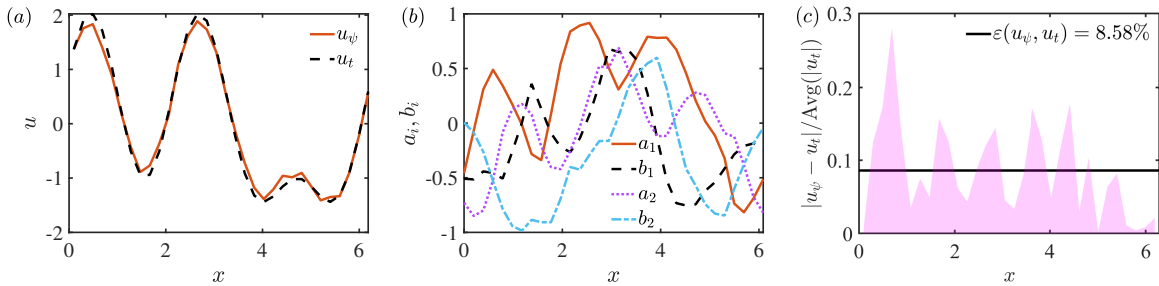


FIGURE 6 Results for generating the spinor field for $u_t = \sin x + \cos 2x + \sin 3x$. (a) Comparison between the target velocity u_t (black dashed line) and the quantum optimization result u_ψ (red solid line). (b) Four real components of the spinor $\psi = [a_1 + b_1 i, a_2 + b_2 i]^T$. (c) Relative error $|u_\psi - u_t| / \text{Avg}(|u_t|)$ (pink shade), with the average relative error $\varepsilon(u_\psi, u_t)$ (black solid line).

For a more intricate target velocity $u_t(x) = \sin x + \cos 2x + \sin 3x$ with multiple Fourier modes, the results in Fig. 6 demonstrates that our algorithm effectively synthesizes a continuous spinor field, achieving close approximation of the target velocity with a relative error of $\epsilon = 8.58\%$.

4.2 | 2D velocity fields

We construct the quantum circuit for a 2D velocity field $\mathbf{u}_t = [\cos x \sin y, \sin x \cos y]$. Note that the velocity components are coupled and exhibit diverse flow structures, such as sources, sinks, and saddle points.

Figure 7(a) shows an excellent agreement between the quantum optimization result and the target field. The low relative error of 4.50% (see Tab. 1) demonstrates the capability of our algorithm in preparing quantum states for the velocity fields based on the spinor field with dimensional coupling. Furthermore, we visualize the streamlines

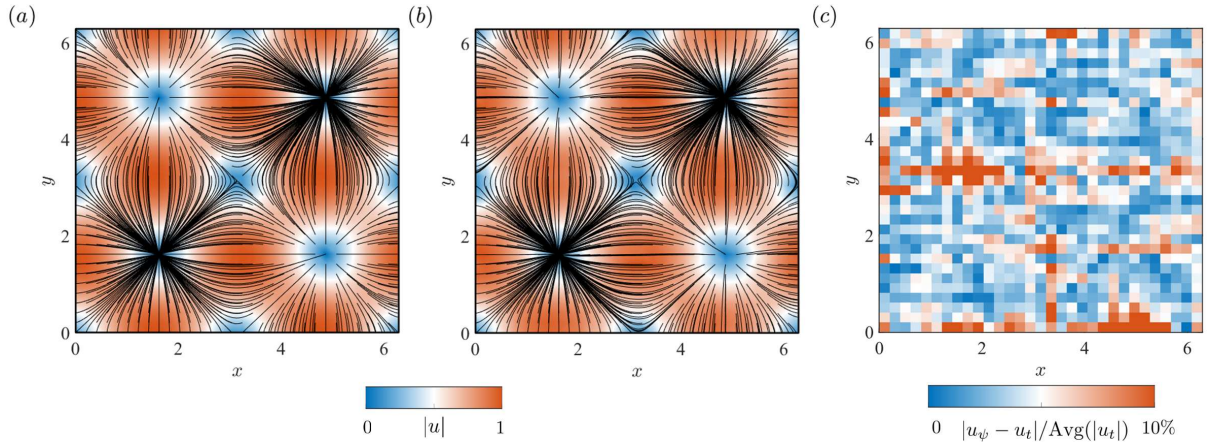


FIGURE 7 Results for generating the spinor field for $\mathbf{u}_t = [\cos x \sin y, \sin x \cos y]$. Streamlines of (a) \mathbf{u}_t and (b) \mathbf{u}_ψ , along with the contours of $|\mathbf{u}_t|$ and $|\mathbf{u}_\psi|$, respectively. (c) Distribution of relative error $|\mathbf{u}_\psi - \mathbf{u}_t| / \text{Avg}(|\mathbf{u}_t|)$, with average relative error of 4.50%.

of both \mathbf{u}_t and \mathbf{u}_ψ in Figs. 7(a) and 7(b). Our algorithm successfully reproduces the intricate flow patterns induced by multiple sources, sinks, and saddle points.

Furthermore, we investigate a more complex velocity field with asymmetric vortices, as shown in Fig. 8(b), where the vortical flow field data is obtained from the evolution of an incompressible Schrödinger flow^{26,47}. The original flow field is presented in Fig. 8(a), where four asymmetric large vortices are located at the four corners of the flow domain. This flow field is more complex to analyze and encode, as it contains more information due to the lack of symmetry. The corresponding optimization result is shown in Fig. 8(b). The deviations are larger than in the previous case due to the increased complexity of the flow. Despite these challenges, the optimization still captures the essential features of the flow, including vortices and their surrounding flows, and demonstrating the algorithms robustness in handling more intricate vortex dynamics.

4.3 | Application to simulating the Schrödinger flow

The quantum circuit and the corresponding quantum states can be utilized for further dynamical evolution. By employing the generalized Madelung transform, the hydrodynamic Schrödinger equation²¹ for the wavefunction ψ under a real potential V corresponds to the compressible Euler equation with an artificial body force, which is detailed in Appendix B.

In the case of $V = 0$, the hydrodynamic Schrödinger equation can be solved by spectral method, which could be conveniently realized by quantum circuit²⁸. More details are provided in Appendix B. The quantum algorithm, as described in Eq. (B11), is implemented in Python with Qiskit. For simulating the Schrödinger flow^{23,21}, we use the initial velocity field shown in Fig. 7, which is applied in the Euler equation in Eq. (B9). The simulation is run for

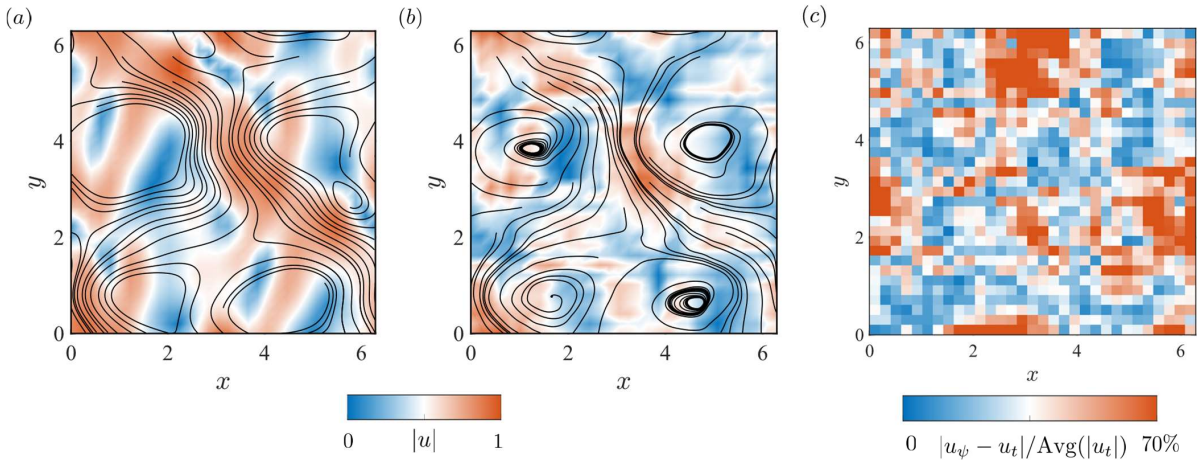


FIGURE 8 Results for generating the spinor field for a complex flow with asymmetric vortices. Streamlines of (a) u_t and (b) u_ψ , along with the contours of $|u_t|$ and $|u_\psi|$, respectively. (c) Distribution of relative error $|u_\psi - u_t| / \text{Avg}(|u_t|)$, with average relative error of 37.53%.

279 two time steps: $t = \pi/3$ and $t = 2\pi/3$. The results are shown in the first row of Fig. 9, where the simulation captures
 280 the interaction of multiple vortices.

281 We also examine the effect of quantum noises on the simulation, which is an inherent challenge in the implemen-
 282 tation of quantum algorithms⁵⁵. Specifically, we consider depolarizing and Pauli errors, these noises are modeled
 283 with error probabilities of 0.01% in Qiskit. The simulation outcomes, displayed in the second row of Fig. 9, demon-
 284 strate consistent agreement between noisy and ideal results at $t = \pi/3$. As the simulation progresses to $t = 2\pi/3$,
 285 noise-induced deviations become apparent yet fail to obscure key flow features, vortical structures and saddle
 286 points remain clearly identifiable. Such resilience against quantum noise highlights the algorithm's capability to
 287 reliably reproduce fundamental flow characteristics despite minor quantitative inaccuracies.

288 5 | CONCLUSIONS

289 We develop a quantum state encoding method for constructing the spinor field corresponding to a given vector
 290 field representing a velocity field in fluid dynamics, with natural extensions to general multidimensional vector
 291 fields in other physical contexts. Leveraging the pointwise normalization constraint of the spinor, we design a
 292 quantum circuit characterized by Hadamard transformations and parameterized controlled rotation gates. Employ-
 293 ing the VQA, we iteratively optimize the circuit parameters to facilitate the transformation of the target velocity
 294 field into the spinor field, thereby enabling subsequent quantum simulation of fluid dynamics. Through 1D and 2D
 295 case studies, we validate the accuracy and robustness of our method, highlighting its effectiveness in handling mul-
 296 tiscale and multidimensional velocity fields. In particular, our method is able to capture essential flow topology,
 297 including sources, sinks, saddle points, and vortices, which characterize complex dynamical systems.

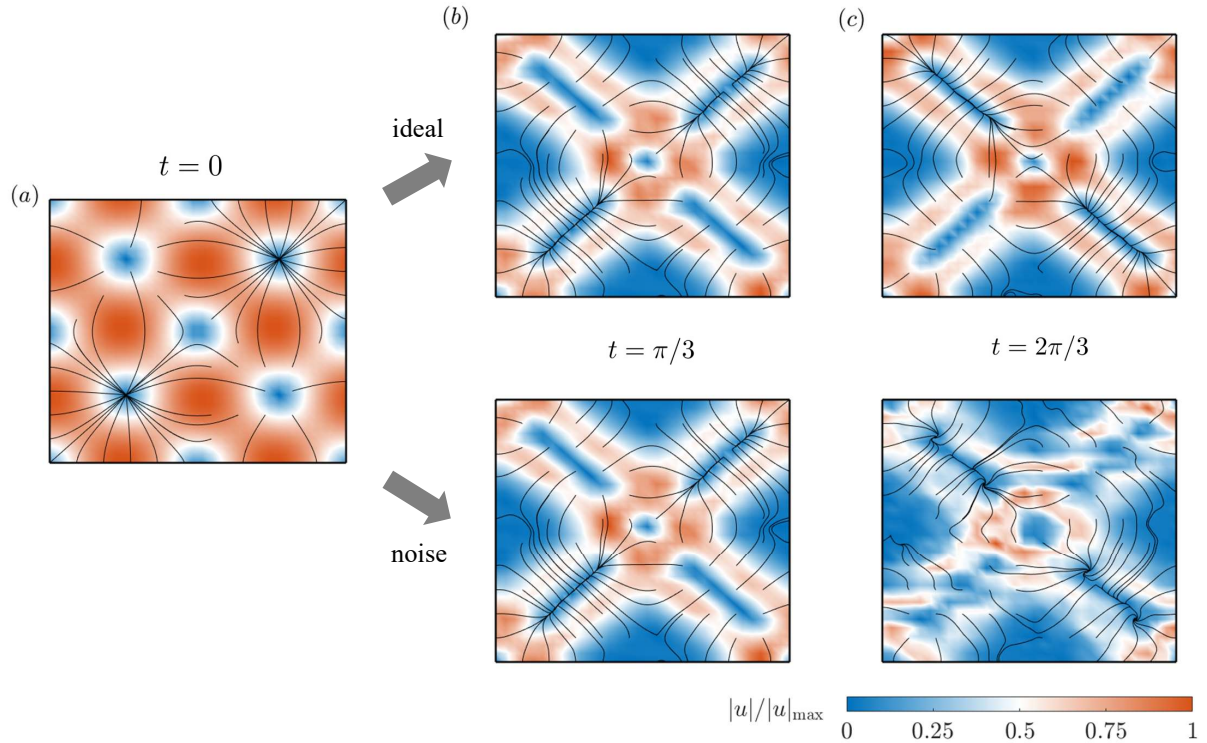


FIGURE 9 Evolution of the Schrödinger flow described by Eq. (B9). The initial condition is shown in Fig. 7. The two columns correspond to results at times $t = \pi/3$ (left) and $t = 2\pi/3$ (right). The first row presents the ideal simulation outcomes, while the second row illustrates the results with quantum noises.

298 To demonstrate the potential of our quantum state encoding method in QCFC, the constructed spinor field is
 299 used as the initial state in the quantum simulation of the Schrödinger flow^{21,22}. While challenges such as quantum
 300 noise remain, the results suggest that quantum computing holds significant potential for simulating complex flow
 301 problems.

302 While our designed quantum circuit has demonstrated its effectiveness through extensive classical simulations,
 303 practical implementation on quantum hardware faces challenges due to decoherence, noise-induced errors, as well
 304 as quantum measurement performed on all qubits, which may lead to inaccuracies and inefficiency. The training of
 305 circuit parameters encounters exponential complexity growth, as $O(N^d)$ operations are inevitable for loss function
 306 calculation for each steps, and extending applications to more complex systems (e.g., 3D flows) requires significant
 307 computational resources. Evaluation of loss function currently experiences increased complexity due to the gradi-
 308 ent term, which can be potentially improved through various approaches, such as parameter-shift rules or refining
 309 the expression of loss function. Advancements in quantum hardware may also facilitate the real implementation of
 310 our method. With development of noise-resilient qubits^{56,57}, high-fidelity quantum gates^{58,59} and various quantum
 311 error correction (QEC) techniques^{60,61,62}, reliable execution of quantum circuits with larger depths will become

312 feasible, leading to realization our method on real quantum hardware as well as more flexible circuit designs. More-
313 over, further progress in data transfer techniques such as quantum random access memory (QRAM)^{63,64,65} will
314 enable efficient data loading and retrieval, which can significantly reduce our measurement complexity and simplify
315 the implementation of our method.

316 Future work will focus on advancing spinor-based QCDF methods^{21,28} by: (1) developing scalable state prepara-
317 tion algorithms for large-scale 3D flows through improved loss functions and quantum computing acceleration; (2)
318 applying the constructed initial states to enhance evolutionary algorithms and quantum measurement techniques;
319 (3) validating quantum state effectiveness for real viscous flow simulations; and (4) extending spinor encoding to
320 vector fields in diverse continuous media including magnetic fluids and elastic materials.

321 AUTHOR CONTRIBUTIONS

322 Hao Su: Formal analysis, Visualization, Writing original draft, Validation. Shiying Xiong: Methodology, For-
323 mal analysis, Funding acquisition, Writing original draft. Yue Yang: Formal analysis, Funding acquisition, Project
324 administration, Supervision, Writing reviews & editing.

325 ACKNOWLEDGMENTS

326 The authors thank C. Song for helpful comments. This work has been supported in part by the National Na-
327 tural Science Foundation of China (Nos. 12432010, 12525201, 12588201, and 12302294), the National Key R&D
328 Program of China (Grant No. 2023YFB4502600), and the New Cornerstone Science Foundation through the
329 XPLORE PRIZE.

330 FINANCIAL DISCLOSURE

331 None reported.

332 CONFLICT OF INTEREST

333 The authors declare no potential conflict of interests.

334 CODE AVAILABILITY

335 The codes for this study are available for download at <https://github.com/YYgroup/SpinorField>.

336 REFERENCES

- 337 1. Steane A. Quantum computing. *Rep. Prog. Phys.*. 1998;61:117.
- 338 2. Nielsen MA, Chuang IL. *Quantum Computation and Quantum Information*. Cambridge University Press, 2010.
- 339 3. Horowitz M, Grumblin E. *Quantum computing: progress and prospects*. National Academies Press, 2019.
- 340 4. Wang Z, Wang X. Quantum-Classical Hybrid Genetic Evolutionary Algorithm for Topology Optimization of Continuum Structures. *International Journal for Numerical Methods in Engineering*. 2025;126.
- 341 5. Cao Y, Romero J, Olson JP, et al. Quantum chemistry in the age of quantum computing. *Chem. Rev.*. 2019;119:1085.
- 342 6. Wittek P. *Quantum machine learning: what quantum computing means to data mining*. Academic Press, 2014.
- 343 7. Mavroeidis V, Vishi K, Zych MD, Jøsang A. The impact of quantum computing on present cryptography. *arXiv preprint arXiv:1804.00200*. 2018.

- 346 8. Jin S, Liu N, Yu Y. Quantum simulation of partial differential equations: Applications and detailed analysis. *Phys. Rev. A*.
347 2023;108:032603.
- 348 9. Xiao Y, Yang LM, Shu C, et al. Physics-informed quantum neural network for solving forward and inverse problems of partial
349 differential equations. *Phys. Fluids*. 2024;36.
- 350 10. Xu YC, Yang J, Kuang ZT, Huang Q, Huang W, Hu H. Quantum computing enhanced distance-minimizing data-driven
351 computational mechanics. *Comput. Methods Appl. Mech. Eng.*. 2024;419:116675.
- 352 11. Jin S, Liu H, Osher S, Tsai YHR. Computing multivalued physical observables for the semiclassical limit of the Schrödinger
353 equation. *J. Comput. Phys.*. 2005;205:222–241.
- 354 12. Aoki S, Endo K, Matsuda Y, Seki Y, Tanaka S, Muramatsu M. Formulation of Correction Term in QUBO Form for Phase-Field
355 Model. *International Journal for Numerical Methods in Engineering*. 2025;126:489–509.
- 356 13. Gaitan F. Finding flows of a Navier-Stokes fluid through quantum computing. *NPJ Quantum Inf.*. 2020;6:61.
- 357 14. Steijl R. Quantum algorithms for fluid simulations. *Advances in Quantum Communication and Information*. 2019;31.
- 358 15. Chen ZY, Ma TY, Ye CC, et al. Enabling large-scale and high-precision fluid simulations on near-term quantum computers. *Comput.
359 Methods Appl. Mech. Eng.*. 2024;432:117428.
- 360 16. Griffin KP, Jain SS, Flint TJ, Chan WHR. Investigations of quantum algorithms for direct numerical simulation of the Navier-Stokes
361 equations. *Center for Turbulence Research Annual Research Briefs*. 2019;347.
- 362 17. Jin S, Li X, Liu N, Yu Y. Quantum simulation for partial differential equations with physical boundary or interface conditions. *J.
363 Comput. Phys.*. 2024;498:112707.
- 364 18. Zhu C, Wang Z, Xiong S, Zhao Y, Yang Y. Quantum implicit representation of vortex filaments in turbulence. *J. Fluid Mech.*.
365 2025;1014:A31.
- 366 19. Ray N, Banerjee T, Nadiga B, Karra S. On the Viability of Quantum Annealers to Solve Fluid Flows. *Front Mech. Eng.*.
367 2022;8:906696.
- 368 20. Pfeffer P, Heyder F, Schumacher J. Hybrid quantum-classical reservoir computing of thermal convection flow. *Phys. Rev. Res.*.
369 2022;4:033176.
- 370 21. Meng ZY, Yang Y. Quantum computing of fluid dynamics using the hydrodynamic Schrödinger equation. *Phys. Rev. Research*.
371 2023;5:033182.
- 372 22. Meng ZY, Yang Y. Quantum spin representation for the Navier-Stokes equation. *Phys. Rev. Research*. 2024;6:043130.
- 373 23. Chern A, Knöppel F, Pinkall U, Schröder P, Weißmann S. Schrödinger's smoke. *ACM Trans. Graph.*. 2016;35:77.
- 374 24. Chern A, Knöppel F, Pinkall U, Schröder P. Inside fluids: Clebsch maps for visualization and processing. *ACM Trans. Graph.*.
375 2017;36:142.
- 376 25. Yang S, Xiong S, Zhang Y, Feng F, Liu J, Zhu B. Clebsch gauge fluid. *ACM Trans. Graph.*. 2021;40:99.
- 377 26. Xiong S, Wang Z, Wang M, Zhu B. A Clebsch method for free-surface vortical flow simulation. *ACM Trans. Graph.*. 2022;41:4.
- 378 27. Tao R, Ren H, Tong Y, Xiong S. Construction and evolution of knotted vortex tubes in incompressible Schrödinger flow. *Phys.
379 Fluids*. 2021;33:077112.
- 380 28. Meng Z, Zhong J, Xu S, et al. Simulating unsteady fluid flows on a superconducting quantum processor. *Commun. Phys.*.
381 2024;7:349.
- 382 29. Hopf H. Über die Abbildungen der dreidimensionalen Sphäre auf die Kugelfläche. *Math. Ann.*. 1931;104:637–665.
- 383 30. Xiong S, Yang Y. The boundary-constraint method for constructing vortex-surface fields. *J. Comput. Phys.*. 2017;339:31–45.
- 384 31. Benedetti M, Lloyd E, Sack S, Fiorentini M. Parameterized quantum circuits as machine learning models. *Quantum Sci. Technol.*.
385 2019;4:043001.
- 386 32. Jaksch D, Givi P, Daley AJ, Rung T. Variational quantum algorithms for computational fluid dynamics. *AIAA J.*. 2023;61:1885–
387 1894.
- 388 33. Codes available at <https://github.com/YYgroup/SpinorField>. 2025.

- 389 34. Gunlycke D, Palenik MC, Emmert AR, Fischer SA. Efficient algorithm for generating Pauli coordinates for an arbitrary linear
390 operator. *arXiv preprint arXiv:2011.08942*. 2020.
- 391 35. Sato Y, Kondo R, Koide S, Takamatsu H, Imoto N. Variational quantum algorithm based on the minimum potential energy for
392 solving the Poisson equation. *Phys. Rev. A*. 2021;104:052409.
- 393 36. Gnanasekaran A, Surana A. Efficient variational quantum linear solver for structured sparse matrices. In: . 1. 2024:199–210.
- 394 37. Demirdjian R, Hogancamp T, Gunlycke D. An Efficient Decomposition of the Carleman Linearized Burgers' Equation. *arXiv
395 preprint arXiv:2505.00285*. 2025.
- 396 38. Bae J, Yoo G, Nakamura S, Ohnishi S, Kim DS. Hardware efficient decomposition of the Laplace operator and its application to
397 the Helmholtz and the Poisson equation on quantum computer. *Quantum Inf. Process.* 2024;23:270.
- 398 39. Cartan É. *The theory of spinors*. Courier Corporation, 1981.
- 399 40. Steane AM. An introduction to spinors. *arXiv preprint arXiv:1312.3824*. 2013.
- 400 41. Andreev PA. Separated spin-up and spin-down quantum hydrodynamics of degenerated electrons: Spin-electron acoustic wave
401 appearance. *Phys. Rev. E*. 2015;91:033111.
- 402 42. Kuznetsov E, Mikhailov A. On the topological meaning of canonical Clebsch variables. *Physics Letters A*. 1980;77:37–38.
- 403 43. Bloch F. Nuclear induction. *Phys. Rev.*. 1946;70:460.
- 404 44. Yang Y, Pullin DI. On Lagrangian and vortex-surface fields for flows with Taylor–Green and Kida–Pelz initial conditions. *J. Fluid
405 Mech.*. 2010;661:446–481.
- 406 45. Yang Y, Pullin DI. Evolution of vortex-surface fields in viscous Taylor–Green and Kida–Pelz flows. *J. Fluid Mech.*. 2011;685:146–
407 164.
- 408 46. Tong Y, Xiong S, He X, Pan G, Zhu B. Symplectic neural networks in Taylor series form for Hamiltonian systems. *J. Comput.
409 Phys.*. 2021;437:110325.
- 410 47. Chern A. *Fluid dynamics with incompressible Schrödinger flow*. PhD thesis. California Institute of Technology, 2017.
- 411 48. Ilya L, Frank H. Decoupled Weight Decay Regularization. *arXiv preprint arXiv:1711.05101*. 2019.
- 412 49. Shende VV, Markov IL, Bullock SS. Minimal universal two-qubit controlled-NOT-based circuits. *Phys. Rev. A*. 2004;69:062321.
- 413 50. Li J, Yang X, Peng X, Sun CP. Hybrid quantum-classical approach to quantum optimal control. *Phys. Rev. Lett.*. 2017;118:150503.
- 414 51. Lockwood O. An empirical review of optimization techniques for quantum variational circuits. *arXiv preprint arXiv:2202.01389*.
415 2022.
- 416 52. McClean JR, Boixo S, Smelyanskiy VN, Babbush R, Neven H. Barren plateaus in quantum neural network training landscapes.
417 *Nat. Commun.*. 2018;9:4812.
- 418 53. Martín EC, Plekhanov K, Lubasch M. Barren plateaus in quantum tensor network optimization. *Quantum*. 2023;7:974.
- 419 54. Liu Z, Yu LW, Duan LM, Deng DL. Presence and absence of barren plateaus in tensor-network based machine learning. *Phys. Rev.
420 Lett.*. 2022;129:270501.
- 421 55. Clerk AA, Devoret MH, Girvin SM, Marquardt F, Schoelkopf RJ. Introduction to quantum noise, measurement, and amplification.
422 *Rev. Mod. Phys.*. 2010;82:1155–1208.
- 423 56. Gyenis A, Paolo AD, Koch J, Blais A, Houck AA, Schuster DI. Moving beyond the transmon: Noise-protected superconducting
424 quantum circuits. *PRX Quantum*. 2021;2:030101.
- 425 57. Cai ZY, Babbush R, Benjamin SC, et al. Quantum error mitigation. *Rev. Mod. Phys.*. 2023;95:045005.
- 426 58. Rower DA, Ding L, Zhang H, et al. Suppressing counter-rotating errors for fast single-qubit gates with fluxonium. *PRX Quantum*.
427 2024;5:040342.
- 428 59. Zhou YC, Ma RL, Kong ZZ, et al. High-fidelity geometric quantum gates exceeding 99.9% in germanium quantum dots. *Nat.
429 Commun.*. 2025;16:7953.
- 430 60. Knill E, Laflamme R. Theory of quantum error-correcting codes. *Phys. Rev. A*. 1997;55:900.

- 431 61. Krinner S, Lacroix N, Remm A, et al. Realizing repeated quantum error correction in a distance-three surface code. *Nature*.
432 2022;605:669–674.
- 433 62. V. V. Sivak and A. Eickbusch and B. Royer and S. Singh and I. Tsoutsios and S. Ganjam and A. Miano and B. L. Brock and A. Z.
434 Ding and L. Frunzio and others . Real-time quantum error correction beyond break-even. *Nature*. 2023;616:50–55.
- 435 63. Giovannetti V, Lloyd S, Maccone L. Quantum random access memory. *Phys. Rev. Lett.*. 2008;100:160501.
- 436 64. Hann CT, Zou CL, Zhang YX, et al. Hardware-efficient quantum random access memory with hybrid quantum acoustic systems.
437 *Phys. Rev. Lett.*. 2019;123:250501.
- 438 65. Jiang N, Pu YF, Chang W, Li C, Zhang S, Duan LM. Experimental realization of 105-qubit random access quantum memory. *npj
439 Quantum Inf.*. 2019;5:28.
- 440 66. Sim S, Johnson PD, Guzik AA. Expressibility and entangling capability of parameterized quantum circuits for hybrid quantum-
441 classical algorithms. *Adv. Quantum Technol.*. 2019;2:1900070.
- 442 67. Schuld M, Swoke R, Meyer JJ. Effect of data encoding on the expressive power of variational quantum-machine-learning models.
443 *Phys. Rev. A*. 2021;103:032430.
- 444 68. Larocca M, Ju N, Martín DG, Coles PJ, Cerezo m. Theory of overparametrization in quantum neural networks. *Nat. Comput. Sci.*.
445 2023;3:542–551.
- 446 69. Haar A. Der Massbegriff in der Theorie der kontinuierlichen Gruppen. *Ann. Math.*. 1933;34:147–169.
- 447 70. Kullback S, Leibler RA. On information and sufficiency. *Ann. Math. Stat.*. 1951;22:79–86.
- 448 71. Kandala A, Mezzacapo A, Temme K, et al. Hardware-efficient variational quantum eigensolver for small molecules and quantum
449 magnets. *Nature*. 2017;549:242–246.

450 SUPPORTING INFORMATION

451 Additional supporting information may be found in the online version of the article at the publishers website.

How to cite this article: H. Su, S. Xiong, and Y. Yang. Quantum state encoding of vortical flows with the spinor
452 field *Int. J. Numer. Methods Eng.* 2021;00(00):1–18.

453 APPENDIX

454 A CLASSICAL OPTIMIZATION ALGORITHM

455 We provide an overview of the method proposed by Chern *et al.*^{23,47} to solve the inverse problem defined
456 in Eq. (4), utilizing classical iterative optimization. Chern *et al.* employ a Ginzburg–Landau-type (GLT) energy
457 functional

$$458 E_{GLT}(\psi) = \int_{\Omega} \frac{1}{2} \|\nabla^{\eta_0} \psi\|^2 \, dx, \quad \text{with } \|\psi\| = 1, \quad (\text{A1})$$

459 where η_0 represents the 1-form of the velocity field, and the covariant derivative $\nabla^{\eta_0} \psi$ is given by

$$460 \nabla^{\eta_0} \psi = d\psi - i\frac{1}{\hbar} \eta_0 \psi. \quad (\text{A2})$$

461 By defining two projection operators, $P_{\mathbb{C}\psi} \equiv \psi\psi^T$ and $P_{\mathbb{C}\eta\psi} \equiv I - P_{\mathbb{C}\psi}$, the following results can be derived

$$462 P_{\mathbb{C}\psi}(\nabla^{\eta_0} \psi) = \frac{1}{\hbar}(\eta - \eta_0)i\psi, \quad P_{\mathbb{C}\eta\psi}(\nabla^{\eta_0} \psi) = -\frac{1}{2}i\psi \, ds. \quad (\text{A3})$$

463 Using these projections, the GLT energy functional is modified to

$$464 \quad E_{GLT}^\varepsilon(\psi) = \int_\Omega \left[\|P_{\mathbb{C}\psi}(\nabla^{\eta_0}\psi)\|^2 + \varepsilon^2 \|P_{\mathbb{C}j\psi}(\nabla^{\eta_0}\psi)\|^2 \right] dx, \quad \text{with } \|\psi\| = 1, \quad (\text{A4})$$

465 where ε is a small regularization parameter that controls the relative importance of the two components. The first
 466 term accounts for the part of the field variation aligned with the velocity field, while the second term, multiplied
 467 by ε^2 , accounts for the perpendicular variation. The parameter ε is crucial in balancing these two components
 468 during optimization and helps ensure that the resulting solution satisfies both the physical constraints and numerical
 469 stability.

470 This expression can be further simplified using the approximation $\nabla^{\eta_0}\psi_{ij} \approx e^{-i(\eta_0)_{ij}/(2\hbar)}\psi_j - e^{i(\eta_0)_{ij}/(2\hbar)}\psi_i$. The
 471 energy functional then takes the quadratic form

$$472 \quad E_\varepsilon(\psi) = \bar{\psi}^T L^\varepsilon(\psi) \psi, \quad (\text{A5})$$

473 where $L^\varepsilon(\psi)$ is a Hermitian matrix that depends on ψ .

474 Although the energy functional $E^\varepsilon(\psi)$ in Eq. (4) is not second-order, which implies a dependence of $L^\varepsilon(\psi)$ on
 475 ψ , Chern *et al.* treat $L^\varepsilon(\psi)$ as a constant matrix during each iteration. This reduces the minimization problem to a
 476 classical quadratic optimization problem, which is solved iteratively by

$$477 \quad [M_V + \Delta t L^{\varepsilon(k)}(\psi^k)]\psi^{k+1} = M_V\psi^k, \quad (\text{A6})$$

478 where M_V is the vertex mass matrix, and Δt is the step size. By iteratively applying Eq. (A6) with a manually
 479 reduced value of ε at each step, the inverse problem is solved numerically.

480 B QUANTUM SIMULATION OF THE SCHRÖDINGER FLOW

481 Madelung originally proposed a formulation that expresses the Schrödinger equation in a form analogous to
 482 the momentum equation in fluid flow, thereby establishing a connection between quantum mechanics and classical
 483 fluid dynamics. However, this formulation is limited to potential flows with vanishing vorticity. The Madelung's
 484 work was extended to vortical flows by considering wave functions with two components^{23,21}, as in the case of
 485 spinors. For a two-component spinor field $\psi = [\psi_1, \psi_2]^T$, the density ρ and velocity \mathbf{u} can be generalized as

$$486 \quad \rho \equiv \langle \psi, \psi \rangle_{\mathbb{R}}, \quad \mathbf{u} \equiv \frac{\hbar}{m} \frac{\langle \nabla \psi, i\psi \rangle_{\mathbb{R}}}{\langle \psi, \psi \rangle_{\mathbb{R}}}. \quad (\text{B7})$$

487 Here, \mathbf{u}_ψ defined in Eq. (2) corresponds to Eq. (B7) when $\rho = m = 1$.

488 Assuming that both components of ψ satisfy the Schrödinger equation

$$489 \quad i\hbar \frac{\partial}{\partial t} \psi_i = \left(-\frac{\hbar^2}{2m} \nabla^2 + V \right) \psi_i, \quad i = 1, 2, \quad (\text{B8})$$

490 the corresponding momentum equation for the system becomes

$$491 \quad \frac{\partial \mathbf{u}}{\partial t} + \mathbf{u} \cdot \nabla \mathbf{u} = -\frac{1}{\rho} \nabla p - \nabla U + \mathbf{f}, \quad (\text{B9})$$

492 where p represents the pressure, U is the potential, and \mathbf{f} is the external force. These quantities are defined as

$$493 \quad p = \frac{\hbar \zeta \cdot s}{m}, \quad U = \frac{V}{m} - \frac{\hbar^2 |\nabla s|^2}{8m^2 \rho^2}, \quad \mathbf{f} = \frac{\hbar \nabla s \cdot \zeta}{m \rho}, \quad \zeta \equiv -\frac{1}{4} \nabla \cdot \left(\frac{\nabla s}{\rho} \right). \quad (\text{B10})$$

494 Equation (B9) resembles the classical Euler equation for compressible fluids. By reformulating velocity-based
 495 fluid dynamics problems as quantum mechanical systems governed by the hydrodynamic Schrödinger equation,
 496 we can utilize quantum computing for simulating fluid flows. This connection opens up new possibilities for using
 497 quantum devices in fluid dynamics simulations, as explored in²².

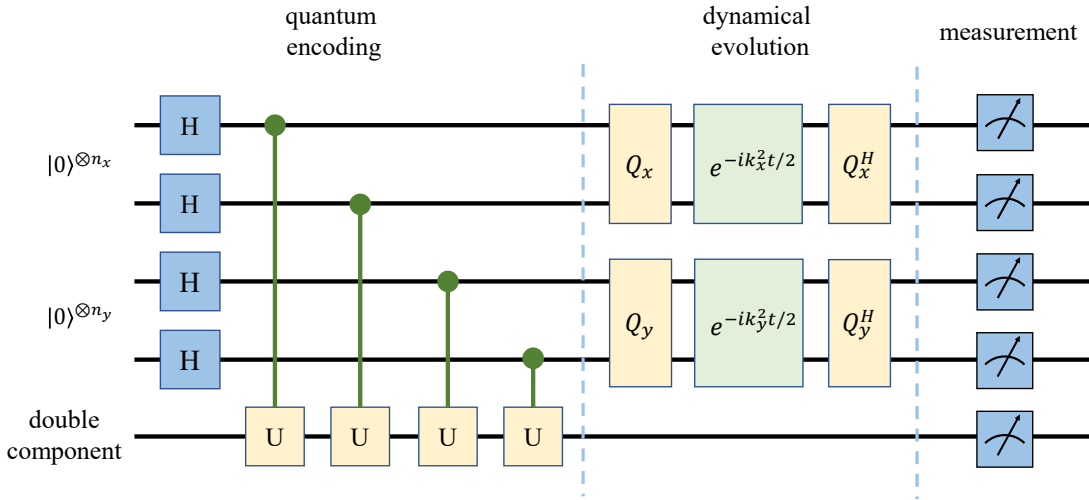


FIGURE B1 General circuit for simulating fluids on quantum device, including the quantum encoding, evolution and measurement. The last qubit encodes the two components for spinor. Quantum encoding utilizes the circuit structure we proposed. Different types of rotation gates are not plotted for simplicity. After quantum encoding, the quantum state is transformed via Eq. (B11), before measurement is performed.

498 The encoded quantum state obtained in Sec. 4 can be used as the initial condition for QCFD. The general circuit
 499 is shown in Fig. B1. We consider the case $V = 0$ in Eq. (B8), which corresponds to the absence of conservative
 500 body forces in the fluid. In this scenario, Eq. (B8) can be solved using a spectral method as

$$501 \quad |\psi(t)\rangle = \left(Q_x^H e^{-ik_x^2 t/2} Q_x \right) \otimes \left(Q_y^H e^{-ik_y^2 t/2} Q_y \right) |\psi(0)\rangle. \quad (\text{B11})$$

502 Here, Q_x and Q_y represent the quantum Fourier transform (QFT) operation:

$$503 \quad Q : |j\rangle \rightarrow \frac{1}{\sqrt{2^n}} \sum_{k=0}^{2^n-1} e^{2\pi i j k / 2^n} |k\rangle. \quad (\text{B12})$$

504 The QFT is known for its polynomial complexity $O(n^2)$, which is exponentially faster than the classical fast Fourier
505 transform (FFT) with complexity $O(n2^n)$. The wavenumber vector $\mathbf{k} = (k_x, k_y)$ in Eq. (B11) is defined as:

$$506 \quad k_i = \text{diag}(0, 1, 2, \dots, 2^{n_i-1} - 2, 2^{n_i-1} - 1, -2^{n_i-1}, \dots, -1), \quad i = x, y. \quad (\text{B13})$$

507 It has been demonstrated that the operators $e^{-ik_x^2 t/2}$ and $e^{-ik_y^2 t/2}$ can be realized using single-qubit gates $R_z(\theta) =$
508 $\text{diag}(e^{-i\theta/2}, e^{i\theta/2})$ and two-qubit gates²⁸

$$509 \quad ZZ(\theta) = \text{diag}(e^{-i\theta/2}, e^{i\theta/2}, e^{i\theta/2}, e^{-i\theta/2}).$$

510 The decomposition has complexity $O(n^2)$. Note that the solution in Eq. (B11) admits a direct computation without
511 iteration steps, as the exponential $e^{-ik^2 t}$ term is directly decomposed.

512 C SENSITIVITY ANALYSIS OF QUANTUM ALGORITHMS

513 We investigate the influence of several critical parameters on the optimization performance with VQA, including
514 the vortex characterization parameter \hbar ²⁴, the number N_g of controlled rotation gates, and the number N of grid
515 points in each dimension. In particular, using the example shown in Fig. 5(a), we tested various parameter values
516 to assess the algorithm's robustness and quantify ranges of the critical parameters. We adjust the parameter values
517 individually to study their influence on spinor field preparation, generally adhering to those listed in Tab. 1. Note
518 that when testing different N values, we chose $N_g = 3$ instead of $N_g = 2$ in Tab. 1 to ensure the quantum circuit's
519 ability to accommodate multi-scale structures with increasing grid size.

520 First, we conduct tests using various values of \hbar , including 0.2, 0.5, 1, 2, and 5. Figure C2 illustrates that when
521 \hbar is within the range of approximately 0.5 to 1, the generated wave function exhibits relatively small errors. This
522 finding is consistent with previous numerical experiments conducted on wave functions^{25,26,23,24}. We remark that
523 even with substantial alterations in the value of \hbar , such as setting $\hbar = 5$, which is 25 times its minimum value,
524 our construction methodology can still capture the large-scale velocity profile. However, larger errors may arise,
525 particularly near the peak velocity.

526 Second, we conduct tests on N_g , which determines the depth of the quantum circuit, i.e., the number of layers
527 of quantum gates. In Fig. C3, when N_g is small, such as $N_g = 1$, the circuit's expressiveness is limited due to the
528 small number of adjustable parameters, resulting in large errors in the output wave function. With a relatively large
529 N_g , such as $N_g = 4$, the circuit contains sufficient adjustable parameters to approximate the target wave function.
530 However, due to the circuit depth and the abundance of parameters, VQA training may encounter challenges like

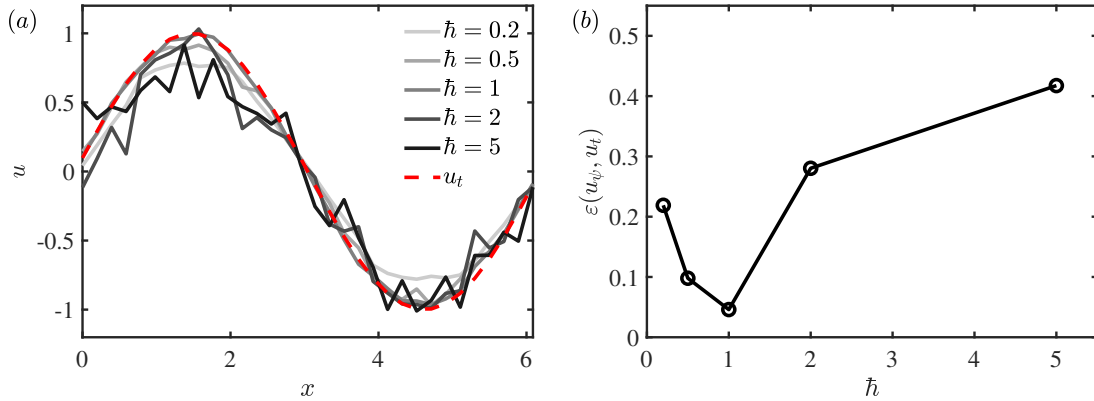


FIGURE C2 Results for generating the spinor field for $u_t = \sin x$ with \hbar varying from 0.2 to 5. (a) Comparison between the target velocity u_t (red dashed line) and the quantum optimization results u_ψ (solid lines). (b) Relative error $\varepsilon(u_\psi, u_t)$ as a function of \hbar .

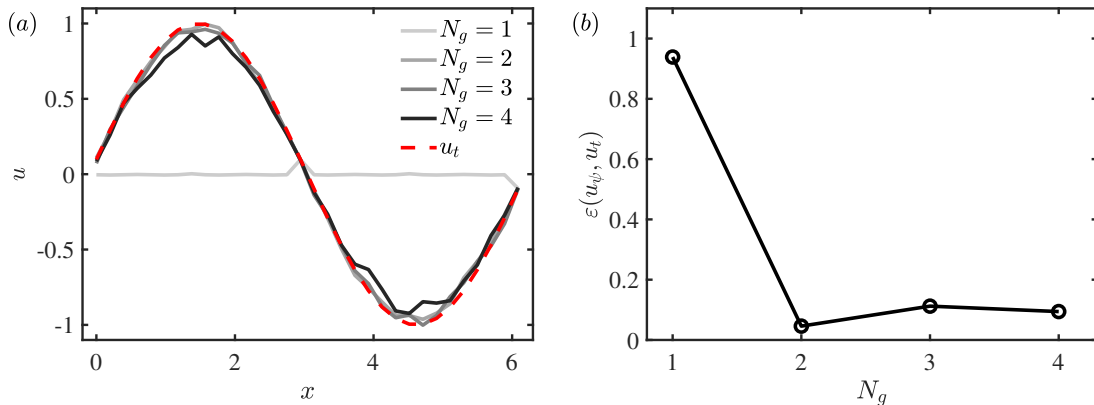


FIGURE C3 Results for generating the spinor field for $u_t = \sin x$ with N_g varying from 1 to 4. (a) Comparison between the target velocity u_t (red dashed line) and the quantum optimization results u_ψ (solid lines). (b) Relative error $\varepsilon(u_\psi, u_t)$ as a function of N_g .

531 the barren plateau^{52,53,54}, which hinders the convergence of parameters and leads to notable errors in the output
 532 wave function. Hence, we suggest a moderate number of quantum circuit layers, such as $N_g = 2$ and 3.

533 Third, we conduct tests on the number of grid points. In Fig. 4(a), the quantum circuit's output wave function
 534 is smoothed with decreasing N , due to the numerical dissipation at low grid resolutions. Conversely, enlarging the
 535 grid size introduces more oscillations, arising from the incorporation of spurious multi-scale information by VQA.
 536 Therefore, it is essential to adjust the grid size to match the characteristic scale of the target velocity field in the
 537 spinor-based quantum state preparation.

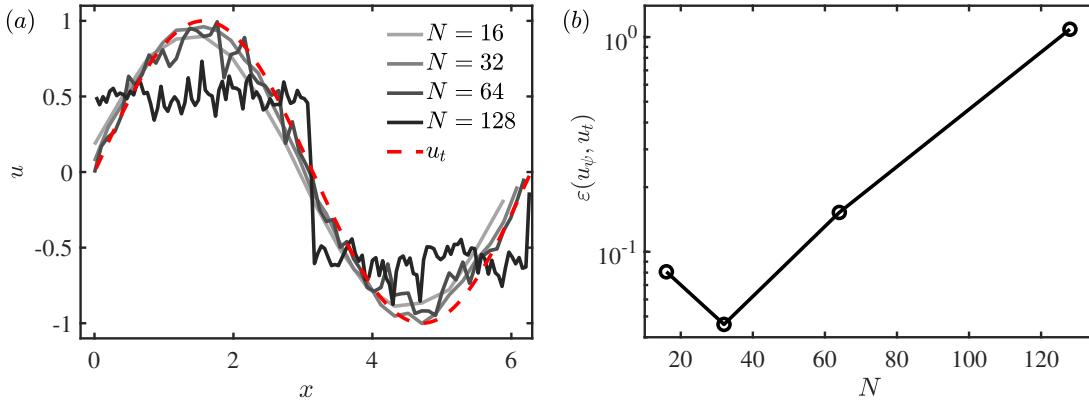


FIGURE C4 Results for generating the spinor field for $u_t = \sin x$ with N varying from 16 to 128. (a) Comparison between the target velocity u_t (red dashed line) and the quantum optimization results u_ψ (solid lines). (b) Relative error $\varepsilon(u_\psi, u_t)$ as a function of N .

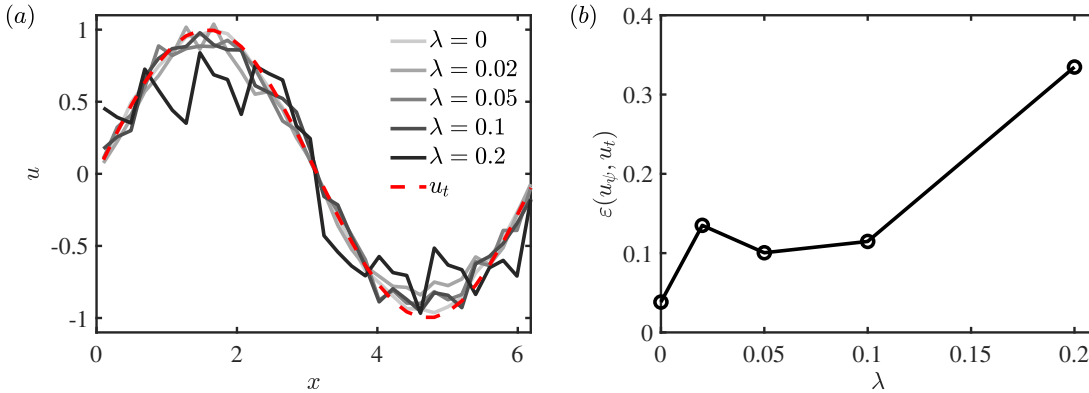


FIGURE C5 Results for generating the spinor field for $u_n(x) = \sin x + \lambda \xi(-1, 1)$, with varying values of λ : 0.02, 0.05, 0.1, 0.2. (a) Comparison between the target velocity $u_t = \sin x$ (red dashed line) and the quantum optimization results u_ψ (solid lines). (b) Relative error $\varepsilon(u_\psi, u_t)$ as a function of λ .

538 Finally, we investigate the effect of noises, which are applied to the target velocity as

539
$$u_n(x) = \sin x + \lambda \xi(-1, 1). \quad (\text{C14})$$

540 Here, $\xi(-1, 1)$ is a random variable uniformly distributed on $[-1, 1]$, and λ controls the amplitude of ξ . In general,
541 the mean error $\varepsilon(u_\psi, u_t)$ grows with λ in Fig. 5(b), where the error is evaluated between the VQA result u_ψ and the
542 undisturbed $u_t(x) = \sin x$.

543 D EVALUATING THE EXPRESSIBILITY OF THE QUANTUM CIRCUIT

544 The expressibility of a parametrized quantum circuit characterizes its ability to explore different states in the
 545 Hilbert space. This is an important factor in the quantum circuit design. Quantification methods for the express-
 546 ibility include the proximity of pairwise fidelity distribution to ideal distribution⁶⁶, the Fourier transform of the
 547 quantum model⁶⁷, and the rank of the Fisher information matrix⁶⁸.

548 We investigate the expressibility of parameterized quantum circuits in terms of the circuit depth, employing
 549 the descriptor based on the fidelity distribution⁶⁶, which is easy for calculation. For a circuit that generates output
 550 states ψ_θ with parameters θ and ψ_ϕ with parameters ϕ , this descriptor evaluates the distribution of state overlaps

$$551 \quad p(F = |\langle \psi_\theta | \psi_\phi \rangle|^2). \quad (\text{D15})$$

552 This distribution quantifies the proximity between two output states derived from the same circuit architecture but
 553 with different parameter sets. It is compared to the distribution over the entire Hilbert space, obtained by randomly
 554 selecting two states, as defined by the Haar measure⁶⁹.

555 The comparison of these distributions is performed using the Kullback–Leibler (KL) divergence⁷⁰, which, in
 556 the discrete setting, is defined as

$$557 \quad D_{KL}(P\|Q) = \sum_i P(i) \log \frac{P(i)}{Q(i)}, \quad (\text{D16})$$

558 where P and Q are two distinct distributions. It can be shown that $D_{KL}(P\|Q) \geq 0$, with values closer to zero
 559 indicating greater similarity between the distributions. Sim *et al.*⁶⁶ computed the divergence

$$560 \quad D_{KL}(p_{PQC}(F)\|p_{Haar}(F)), \quad (\text{D17})$$

561 where $p_{PQC}(F)$ and $p_{Haar}(F)$ refer to the distributions for the parametrized quantum circuit and the entire Hilbert
 562 space, respectively. A value closer to zero indicates a higher expressibility of the parametrized circuit.

563 In our study, to examine a subspace of the Hilbert space with the normalization condition in Eq. (1), we sample
 564 each spinor $[\psi_1, \psi_2]$ as uniformly distributed points on a 3D unit sphere. We consider the case with $n = 6$ qubits
 565 and the number of controlled rotation gates N_g ranging from 1 to 10. The variation of the KL divergence with N_g is
 566 illustrated in Fig. D6. For $N_g = 1$, D_{KL} is relatively large, indicating limited expressibility. For $N_g \geq 2$, D_{KL} exhibits
 567 minimal variation across these cases. These results suggest that increasing the circuit depth does not necessarily
 568 improve the expressibility. Instead, deeper circuits may complicate training due to the barren plateau effect⁵⁴.

569 Furthermore, for $N_g = 2$, the KL divergence is approximately 10^{-3} . According to the experiments on various
 570 quantum circuit structures in Ref.⁶⁶, the best KL divergence achieved was also on the order of 10^{-3} . Hence, it
 571 appears that the $N_g = 2$ case can cover most of the Hilbert space of interest.

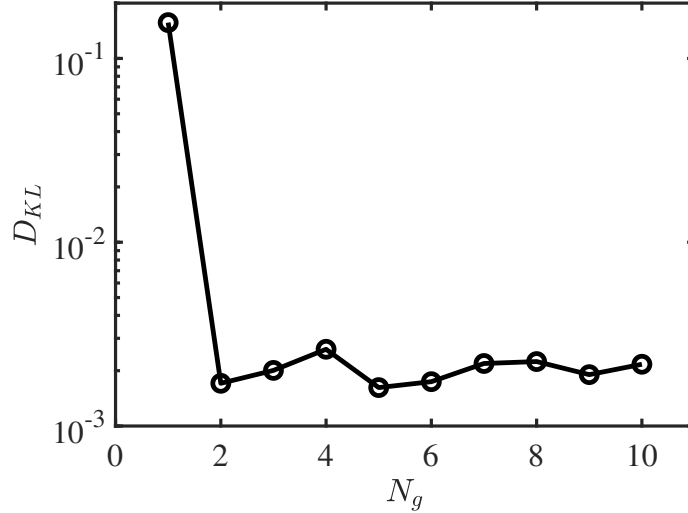


FIGURE D6 The KL divergence D_{KL} between the output space of the proposed quantum circuit and the spinor solution space. The analysis is performed with $n = 6$ qubits, and the gate group number varies from 1 to 10. Each case is sampled 50,000 times.

572 E COMPARISON WITH HARDWARE-EFFICIENT ANSATZ

573 We test the effect of hardware-efficient ansatz⁷¹ by directly encoding the 2D velocity field on quantum state
 574 magnitude, and compare the result with our spinor-based method. In this section, we apply the following encoding

$$575 |\psi\rangle = \frac{1}{\mathcal{N}} \sum_{p=0}^{2^{n_x}-1} \sum_{q=0}^{2^{n_y}-1} (u_x(x_p, y_q) + i u_y(x_p, y_q)) |p\rangle \otimes |q\rangle,$$

576 with total qubit number of n_x+n_y . $u_x(x_p, y_q)$ and $u_y(x_p, y_q)$ refer to the two velocity components on grid point (x_p, y_q) ,
 577 and $\mathcal{N} = \sum_{i,j} |\mathbf{u}|^2$ refers to the normalization coefficient. The ansatz is presented in Fig. E7, which is constructed
 578 by repeated quantum layers. Each quantum layer consists of several R_y and R_z gates, along with controlled-Z gates.

579 We use the ansatz in Fig. E7 to encode the velocity field of Case 4 in Tab. 1, which is the asymmetric vortices.
 580 We apply the VQA method for optimization, and use the straightforward loss function $L = \|\mathbf{u}_\psi - \mathbf{u}_t\|_2^2$. We discretize
 581 the velocity field on a 32×32 grid and encode it with 10 qubits. During the optimization process, the learning
 582 rate is set to 0.001 with 10000 training steps. Four different layer numbers $N_l = 15, 20, 25, 30$ are tested, with
 583 results summarized in Fig. E8. The convergence process is presented in Fig. 8(a), where all four cases converge to
 584 similar loss values, indicating that the $N_l = 15$ is sufficient for this specific velocity field. The final average relative
 585 error, defined in Eq. (12), are shown in Fig. 8(b), with the spinor result $\epsilon = 37.53\%$ as in Tab. 1 also provided for
 586 comparison. These results suggest that our method can obtain a spinor field with a relative error similar to that of
 587 the hardware-efficient ansatz.

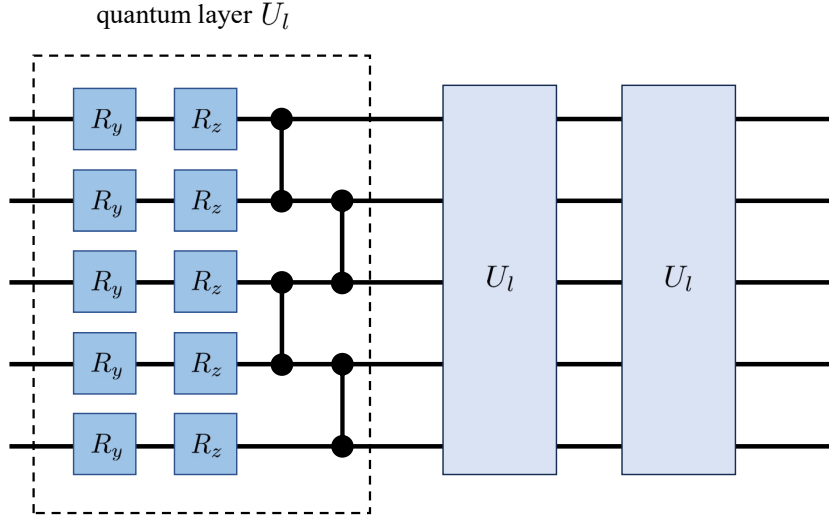


FIGURE E7 The circuit for hardware-efficient ansatz used for testing. One quantum layer consists of several R_y and R_z gates, along with controlled-Z gates. The layer is then repeated several times.

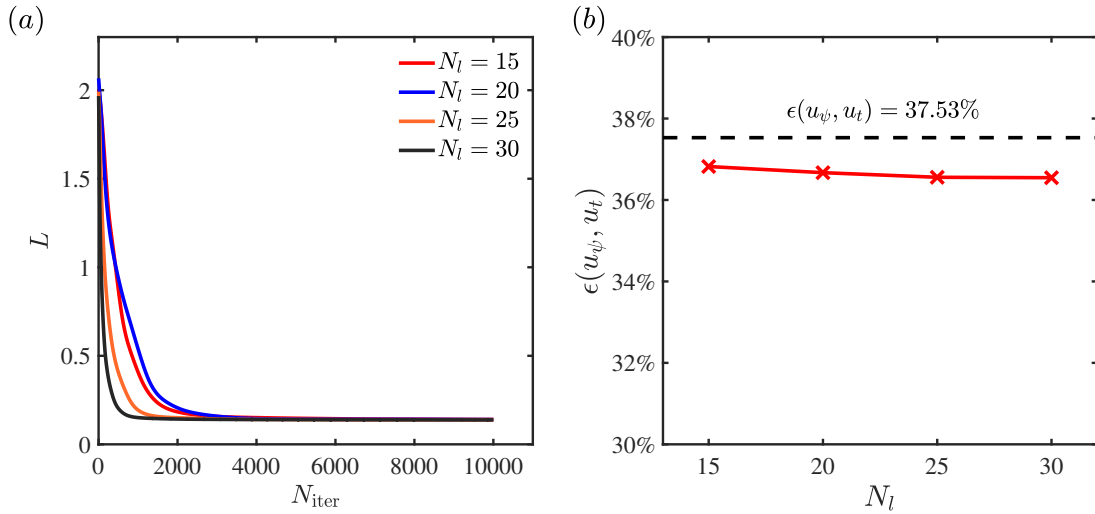


FIGURE E8 VQA result of hardware-efficient ansatz encoding asymmetric vortices with different layer numbers $N_l = 15, 20, 25, 30$. (a) The convergence process of loss function with 10000 iteration steps. (b) The final average relative error for four layer numbers, compared with our spinor field result of 37.53% in Tab. 1.

588 It is worth noting that our spinor method can provide richer information about the inner structure of the given
589 velocity field, and the encoded quantum state can be used for further simulation via the Schrödinger equation.

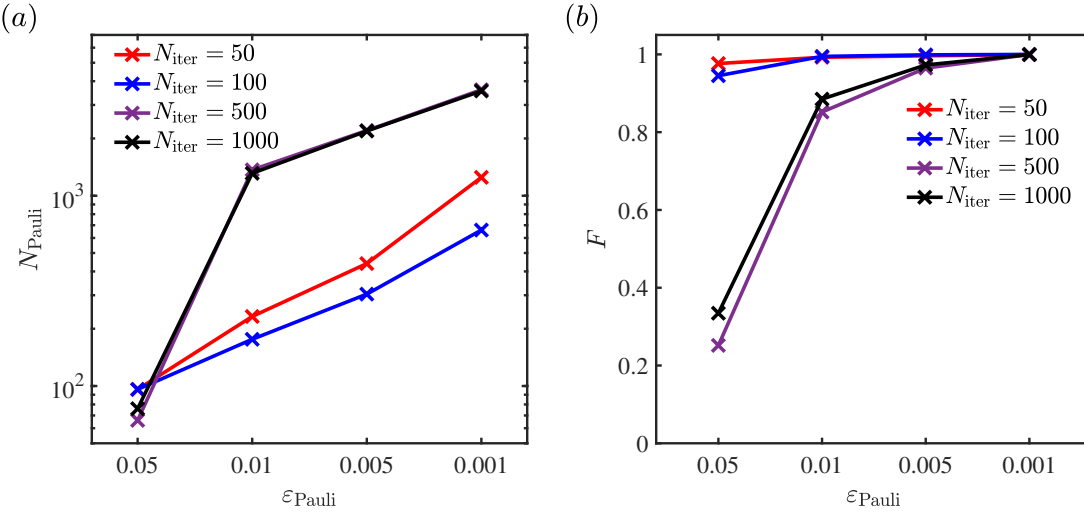


FIGURE F9 Results of Pauli decomposition for spinor fields extracted from iteration steps $N_{\text{iter}} = 50, 100, 500, 1000$ for Case 1. The Pauli strings are trimmed with four different threshold values $\varepsilon_{\text{Pauli}} = 0.05, 0.01, 0.005, 0.001$. (a) shows the number of Pauli strings retained after trimming. (b) shows the fidelity F between original spinor field and the reconstructed quantum state.

590 F NUMERICAL ANALYSIS ON COMPLEXITY OF PAULI DECOMPOSITION

591 We numerically analyze the complexity of Pauli decomposition implemented on the measurement of the spinor
 592 field ψ during the optimization process. As examples, we choose four different spinor fields extracted from four
 593 iteration steps, $N_{\text{iter}} = 50, 100, 500, 1000$ during Case 1, with a qubit number of $n = 6$. For each of these spinor
 594 fields, we calculate $4^n = 4096$ Pauli decomposition coefficients c_σ as

$$595 \quad c_\sigma = \frac{1}{2^n} \text{Tr}(\sigma |\psi\rangle \langle \psi|), \quad (\text{F18})$$

596 where $\sigma \in \{I, X, Y, Z\}^{\otimes n}$ denotes random Pauli string, and Tr is the trace operator. We then set a threshold value
 597 $\varepsilon_{\text{Pauli}} \in (0, 1)$ and retain Pauli strings with coefficients greater than the threshold value, with the approximate
 598 density matrix $\tilde{\rho}$ reconstructed as

$$599 \quad \tilde{\rho} = \sum_{|c_\sigma| \geq \varepsilon_{\text{Pauli}}} c_\sigma \sigma. \quad (\text{F19})$$

600 The number of Pauli strings retained is denoted as N_{Pauli} . Here, we take the first row vector of $\tilde{\rho}$, denoted as $\tilde{\psi}$, as
 601 an approximation of the original spinor field. We then use the fidelity $F = |\langle \tilde{\psi} | \psi \rangle|^2$ to observe the accuracy of the
 602 reconstruction.

603 For the four spinor fields described above, we use four different threshold values $\varepsilon_{\text{Pauli}} = 0.05, 0.01, 0.005, 0.001$
 604 to trim the Pauli strings, with results demonstrated in Fig. F9. It's noticed that during the early stages of the opti-
 605 mization, where the loss function varies rapidly, the spinor field ψ can be approximated with good accuracy even

606 with a high threshold value and Pauli string number below 100, which implies potential speedup of measurement
607 by Pauli decomposition. However, as the optimization process progresses, lower threshold values are required to
608 maintain high quantum fidelity, which also brings larger N_{Pauli} . The result suggests that Pauli decomposition has
609 the potential of providing considerable speedup during early stage of the optimization process, where the loss func-
610 tion decreases the most rapidly. In the later stages of optimization, the speedup is weaker and the measurement
611 might require more resources. A general combination of Pauli strings applicable to all possible spinor fields is
612 worth exploring further in future work.